

Research Article

Dislocation Analysis of 3C-SiC Nanoindentation with Different Crystal Plane Groups Based on Molecular Dynamics Simulation

Dongling Yu ^{1,2}, Huiling Zhang ^{1,3}, Jiaqi Yi ^{1,3}, Yongzhen Fang ^{1,3}
and Nanxing Wu ^{1,2,3}

¹School of Mechanical and Electronic Engineering, Jingdezhen Ceramic Institute, Jingdezhen 333403, China

²National Engineering Research Center for Domestic & Building Ceramics, Jingdezhen 333001, China

³Laboratory of Ceramic Material Processing Technology Engineering, Jingdezhen, 333403 Jiangxi Province, China

Correspondence should be addressed to Nanxing Wu; ldhjdz1987@163.com

Received 20 September 2021; Revised 25 November 2021; Accepted 26 November 2021; Published 15 December 2021

Academic Editor: Hui Yao

Copyright © 2021 Dongling Yu et al. This is an open access article distributed under the Creative Commons Attribution License, which permits unrestricted use, distribution, and reproduction in any medium, provided the original work is properly cited.

To explore the deformation law of nanoindentation dislocations of different crystal plane groups of 3C-SiC by cube indenter. The molecular dynamics simulation method is used to construct the different crystal plane family models of 3C-SiC, select the ensemble, set the potential function, optimize the crystal structure, and relax the indentation process. The radial distribution function, shear strain, and dislocation deformation of nanoindentation on (001), (110), and (111) planes were analyzed, respectively. In the radial distribution function, the change in $g(r)$ in the (110) crystal plane is the most obvious. Shear strain and dislocation occur easily at the boundary of square indentation defects. During the indentation process, the shear strain is enhanced along the atomic bond arrangement structure, (001) crystal plane shear strain is mainly concentrated around and below the indentation defects and produce a large number of cross dislocations, (110) the crystal plane shear strain is mainly concentrated in the shear strain chain extending around and below the indentation defect, which mainly produces horizontal dislocations, and (111) the crystal plane shear strain is mainly concentrated in four weeks extending on the left and right sides in the direction below the indentation defect and produces horizontal and vertical dislocations. The direction of shear stress release is related to the crystal structure. The crystal structure affects the direction of atomic slip, resulting in the results of sliding in different directions. The final dislocation rings are different, resulting in different indentation results.

1. Introduction

3C-SiC has excellent comprehensive properties such as high strength, high hardness, corrosion resistance, high temperature resistance, and low coefficient of thermal expansion [1, 2] and is widely used in high-precision fields such as aerospace, weapons and equipment, medical devices, and electronic components [3–5]. In the indentation experiment, due to the great hardness of 3C-SiC, it is impossible to monitor various changes in 3C-SiC specimen in real time, and the experiment has great limitations [6, 7]. The internal structures of different crystal planes are quite different [8, 9], and the arrangement structure of microatoms has an important impact on the mechanical properties of 3C-SiC [10–12]. By using molecular dynamics simulation of 3C-SiC nanoindentation, we can effectively analyze the radial distri-

bution function, shear strain, and dislocation deformation of different crystal planes of 3C-SiC in the indentation process.

Nanoindentation has become a common method for studying the mechanical properties of materials. Molecular dynamics (MD) simulation can effectively simulate the overall process of nanoindentation and analyze the data [13–15]. Liang et al. [16, 17] analyzed the elastic-plastic deformation mechanism of single-crystal cubic silicon carbide in spherical nanoindentation by the molecular dynamics method. The indentation defect region composed of amorphous phase and dislocation on the 3C-SiC (010) crystal plane is more obvious than that in the other two (110) and (111) crystal planes. Wu and Zhang [18] studied the effect of amorphous film on 6 h SiC nanoindentation deformation mechanism and mechanical properties by combining

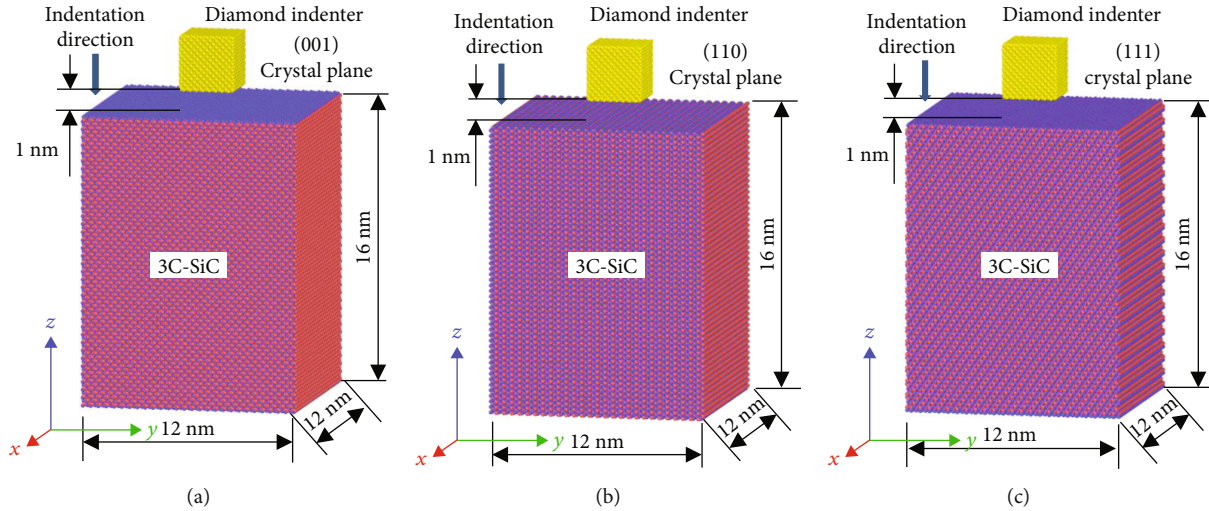


FIGURE 1: Molecular dynamics model of nanoindentation on different faces of 3C-SiC.

experiment and simulation. With the increase of indentation depth, amorphous SiO_2 films densify first and then rupture. The modulus and hardness increase with increasing indentation depth in the initial stage, but finally reach a stable value equivalent to that of single crystal 6h SiC. Pang et al. [19] explored the evolution of the local deformation response of direct and nearby shear strains at the indenter tip and found that the cone slip family contributes greatly to the deformation process. Leide et al. [20] studied indentation deformation using high-resolution electron backscatter diffraction and Raman spectroscopy. It was found that the fracture of the irradiated sample was inhibited by the residual compressive stress of expansion and the plastic deformation region extended outward from the indentation. The effects of indentation depth and indenter tip on dislocation formation and deformation mechanism during nanoindentation were analyzed by molecular dynamics simulation. However, the effect of cube indenter on the shear strain and dislocation deformation of 3C-SiC specimens during indentation is not analyzed from the perspective of crystal structure.

Based on the research of the above scholars on nanoindentation, the cube indentation process on different crystal surfaces of 3C-SiC specimens is analyzed by molecular dynamics simulation. This paper mainly analyzes the influence of cube indenter on the shear strain of atomic structure in crystal and the dislocation deformation. The research results are of guiding significance for the study of the dislocation forming and deformation mechanism in the process of nanoindentation.

2. Physical Model of SiC Indentation Process

2.1. Establishment of MD Model. The indentation surface selects one common crystal surface from three different crystal surface families of $\{100\}$, $\{110\}$, and $\{111\}$ for simulation. In Figures 1(a)–1(c), there are three models established with (001), (110), and (111) crystal surfaces as indentation surfaces, respectively. The 3C-SiC specimen in the model is $12 \text{ nm} \times 12 \text{ nm} \times 16 \text{ nm}$ cuboid. A fixed layer and a constant

temperature layer are, respectively, arranged at the bottom from bottom to top to fix the boundary, reduce the boundary effect, and transfer heat to keep the temperature unchanged. The upper part of the constant temperature layer is a Newton layer. According to the principle of mathematical calculus, the area of the graph surrounded by the curve can be solved by countless rectangles. Indenters of different shapes can also be decomposed into countless small cube indenters, and the diamond indenter is a cube with a side length of 3 nm. The four sides of the indenter are parallel to the corresponding side of the silicon carbide test piece. In order to ensure the reliability and accuracy of nanoindentation molecular dynamics simulation results, the indenter is divided into boundary layer, constant temperature layer, and Newton layer from top to bottom. The lower bottom surface of the indenter is 1 nm away from the indentation surface, and the indenter moves towards 3C-SiC along the negative direction of z -axis.

The simulation parameters are mainly different due to the change of indentation surface, and the atomic number of 3C-SiC specimen has a small gap due to the change of crystal surface. The 3C-SiC specimen with indentation surface of (111) crystal plane has the largest number of atoms, 242272, and there is little difference between the number of atoms of (001) crystal plane and (110) crystal plane. The diamond indenter is a cube with a side length of 3 nm and its atomic number is 4913. The simulated temperature is 900 K, the pressure drop speed is 50 m/s, and the time step is 1 fs. The specific simulation parameters are shown in Table 1 below.

2.2. Establishment of Simulation Environment. In order to stabilize the arrangement of C and Si atoms, the x -axis and y -axis directions are defined as periodic boundary conditions, the indenter moves in the negative direction of z -axis, and the z -axis direction is defined as a contractive free boundary condition. Through the structural optimization and relaxation process, the atoms can maintain equilibrium and stability in the indentation process and are not easy to

TABLE 1: Molecular dynamics simulation parameters.

Parameters	Value
Crystal plane group	{100}, {110}, {111}
Sample indentation surface	(001), (110), (111)
Numbers of atoms in specimen	222338, 223080, 242272
Dimensions of specimen	12.00 nm × 12.00 nm × 16.00 nm
Dimensions of indenter	3.00 nm × 3.00 nm × 3.00 nm
Numbers of indenter	4913
Equilibration temperature	900 K
Indenting speed	50 m/s
Time step	1 fs

collapse and fly out. When selecting the ensemble, the environment required by the relaxation process, and the indentation process is different. The relaxation process requires the temperature of the whole system to remain unchanged, and isothermal isobaric ensemble (NPT) is selected for all layers. During the indentation process, atoms collide violently with each other, resulting in system instability and temperature rise. In order to strengthen the system stability, the Newton layer and constant temperature layer of silicon carbide and diamond adopt microcanonical ensemble (NVE).

In order to make the simulation results consistent with the reality, the combination of Tersoff and vashishta potential functions is used for simulation. Tersoff potential function and vashishta potential function are applied to different regions, respectively. The improved Tersoff potential function of erhart [21] describes the interaction between silicon carbide atoms and diamond atoms more accurately, and the interaction between C atoms in diamond and Si atoms and C atoms in silicon carbide specimen is described by the improved Tersoff potential function. The expression is as follows:

$$E = \frac{1}{2} \sum_{i>j} f_C(r_{ij}) [2V_R(r_{ij}) - (b_{ij} + b_{ji})V_A(r_{ij})], \quad (1)$$

where E is the total energy in the system, f_C is the smooth truncation function, V_R is the duality of repulsion term, V_A is the duality of attraction term, b_{ij} is the bond order function, and r_{ij} is the distance between i atom and j atom.

Vashishta potential function [22] contains two body potential and three body potential. The two body potential contains repulsive force, shielded Coulomb force, shielded charge dipole, and dispersion interaction, and the three body potential contains bond angle energy. The interaction of the two can effectively describe the van der Waals force and covalent bond between Si-C, Si-Si, and C-C atoms in silicon carbide atoms. The expression of vashishta potential function is as follows:

$$V = \sum_{i>j} V_{ij}^{(2)}(r_{ij}) + \sum_{i,j<k} V_{ijk}^{(3)}(r_{ij}, r_{ik}), \quad (2)$$

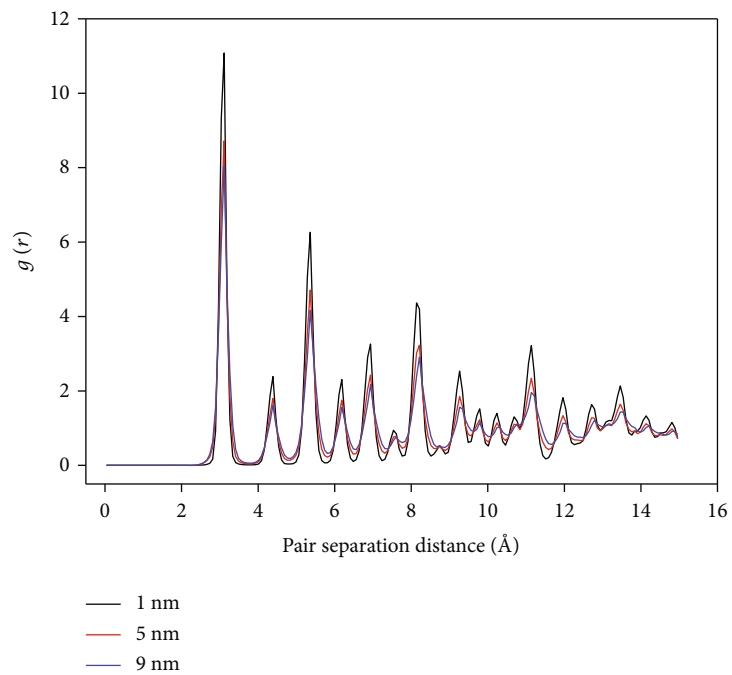
where V is the total energy in the system, V_{ij} is the two body potential, and V_{ijk} is the three body potential.

2.3. Simulation Calculation. The visualization software ovito is used to analyze the nanoindentation process. Atomic strain analysis can effectively analyze von Mises shear strain. Dislocation extraction algorithm (DXA) can accurately identify the dislocations generated in the indentation process and screen the dislocation structure by identifying diamond structure (IDS) analysis method. Adding atomic bonds is more effective to show the force between atoms. Color coding more intuitively shows the shape and structure of dislocation and the strain of interatomic bond.

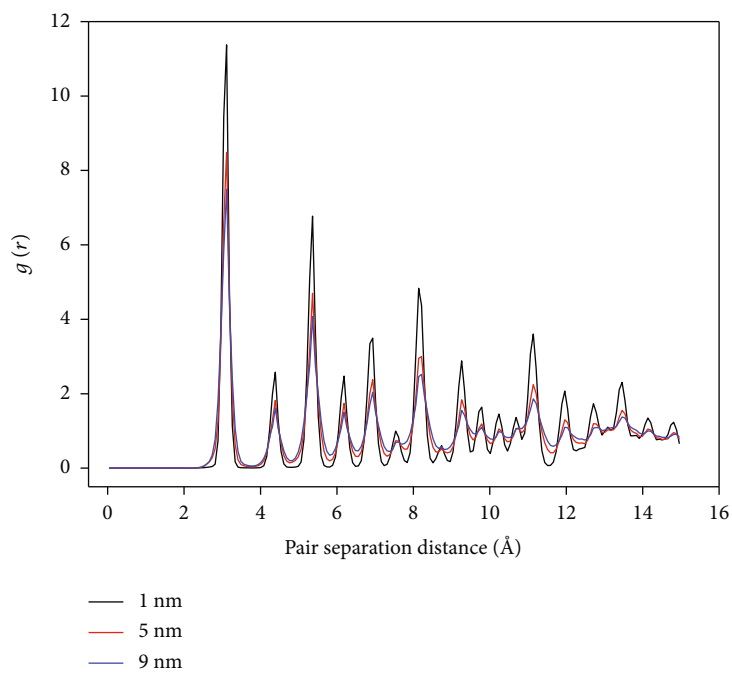
3. Results and Analysis

3.1. Effect of Different Crystal Planes on Radial Distribution. The crystal structures of different crystal planes of 3C-SiC specimens at different indentation depths are analyzed by radial distribution function (RDF). The RDF analysis of Si-Si bond is shown in Figure 2. When the indentation depth is 1 nm, all peaks are steep and the peaks are high. When the depth of the indenter entering the 3C-SiC specimen is half of the height of the indenter, the indentation depth is 1.5 nm. The peak value of $g(r)$ on the (110) crystal plane is slightly larger than that on the other two crystal planes, and the (001) crystal plane basically coincides with $g(r)$ on the (111) crystal plane. At the same indentation depth, the crystal structures of three different crystal planes are similar. At the initial stage of indentation, the number of $g(r)$ peaks did not decrease with the increase of indentation depth. The deformation area of 3C-SiC specimen is small and basically maintains the original crystal structure. With the further increase of indentation depth, when the indentation depth is 9 nm, the curves of three crystal planes at the cutoff radius $r > 12 \text{ \AA}$ are relatively flat, and the number and intensity of $g(r)$ peaks decrease. In the process of nano indentation, the original crystal structure is destroyed to form amorphous silicon carbide, and the adjacent atoms are reduced due to the increase of defects.

3.2. Effect of Different Crystal Planes on Shear Strain. Due to the different arrangement and combination structures of atomic bonds on different crystal planes, the shear strain and deformation produced by the same cube indenter on different crystal planes are also different. Figure 3 shows the shear strain of 3C-SiC specimens with different crystal planes at the same indentation depth of 2.0 nm. Figures 3(a)–3(c), respectively, show the shear strain of two layers of atomic bonds at the intermediate interface perpendicular to the x -axis with the indentation planes (001), (110), and (111), and (d)–(f), respectively, show the shear strain of two layers of atomic bonds at the intermediate interface perpendicular to the y -axis with the indentation planes (001), (110), and (111). Figures 3(g)–3(i) show the overall dislocation bond shear strain diagrams with indentation planes (001), (110), and (111), respectively. The atomic bonds in Figures 3(a) and 3(d) are inclined grid connection structures, but the internal arrangement directions are different.

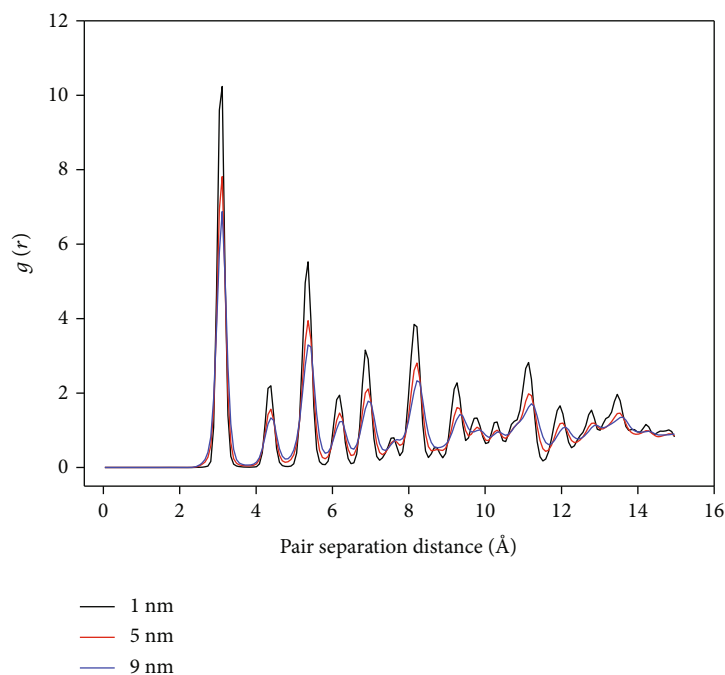


(a) (001) crystal plane

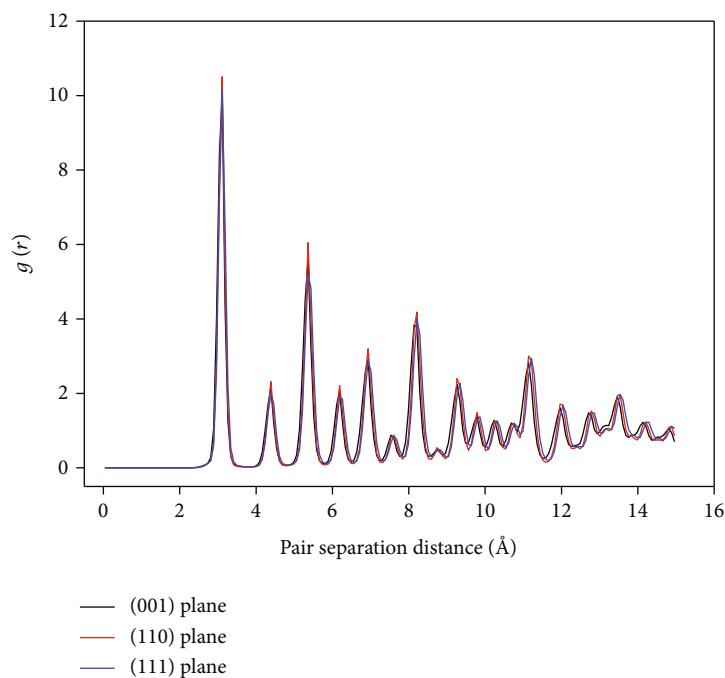


(b) (110) crystal plane

FIGURE 2: Continued.



(c) (111) crystal plane



(d) Indentation depth 1.5 nm

FIGURE 2: RDF analysis of different crystal planes under different indentation depths.

When subjected to the downward pressure from the cube indenter, the shear strain is mainly concentrated directly below and at both ends of the indenter. The atoms at both ends slide towards the middle along the inclined angle of the grid structure, resulting in a small weak strain region directly below the indenter. In Figure 3(d), atoms form a separate prominent shear strain region during the oblique sliding process. The end of the shear strain region of the intermediate interface is a point on the dislocation ring in

Figure 3(g), the ends of all interface strain regions are connected to form a dislocation ring, and there is a weak strain region in the center of the indentation defect (as shown in Figure 3(g)). In Figure 3(b), the atomic bond is a longitudinally arranged connection structure, and in Figure 3(e), the atomic bond is a forward grid structure. The shear strain effects generated during the indentation process are similar. Both of them are that the indentation defect is surrounded by a strong strain region, and no single weak shear strain

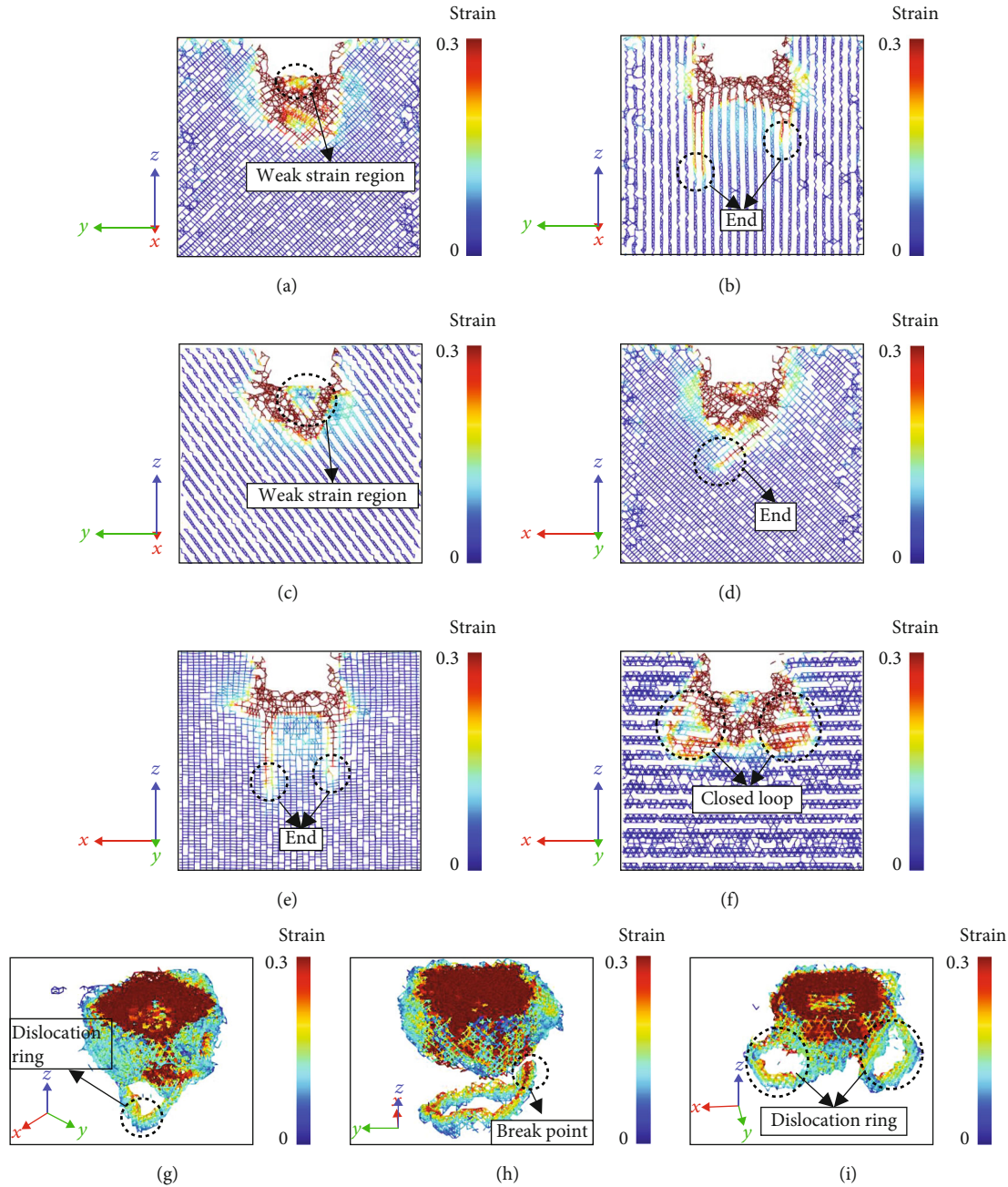


FIGURE 3: Shear strain nephogram at indentation depth of 2.0 nm.

region is generated. With the increase of shear strain, the longitudinal atomic bond below the two ends of the indentation defect releases the shear strain. The ends of the two prominent shear strain regions in Figures 3(b) and 3(e) are on the dislocation ring in Figure 3(h). The shear strain chain with shorter length in Figure 3(b) is the breaking point of the dislocation ring in Figure 3(h). Due to the connection between the dislocation ring and the main body, the shear strain chain at the breaking point is shorter. With the increase of indentation depth, the protruding region will increase, and the dislocation ring will decrease. The side length of the cube indenter remains unchanged, and the length between the two ends of the indentation defect will not change. The ends

of the shear strain region below the two ends are connected to form a rectangular dislocation ring. The atomic bond connection structures in Figures 3(c) and 3(f) are different, and the results produced in the indentation process are quite different. In Figure 3(c), the atomic bond is an oblique connection structure, and a triangular weak strain region appears in the indentation process. The left strong shear strain is distributed along the atomic bond structure chain. The angle between the extension direction of the right strong shear strain and the horizontal line is larger than that on the left. The extension lines on both sides and the bottom of the indentation defect form a triangle where the weak strain region is located. The left strong strain region increases to

both sides along the extension direction, and the area of the left strong strain region is more than that of the right. The nucleation and gliding of dislocations on the left are more than those on the right. In Figure 3(f), the atomic bond is a double-layer transverse connection structure. During the indentation process, the shear strain extends obliquely from both ends of the bottom of the indentation defect to the middle and lower. After the intersection, a triangular weak strain region is formed. The intersecting strong strain region slows down the speed of continuing to extend downward alone and releases to both sides along the transverse structure. A shear strain region extends from both ends of the indentation defect and is connected with the strain region released along the transverse structure to form a closed loop. The shear strain in the closed loop increases. The position of the closed loop is the approximate boundary of the dislocation ring in Figure 3(i), and there is also a weak strain region in the center of the indentation defect in Figure 3(i). In the process of indentation, the nucleation and gliding of dislocations produce shear strain. When the concentrated shear stress reaches the critical value, the release direction of shear stress is related to the crystal structure.

Figure 4 shows the shear strain of 3C-SiC specimens with different crystal planes at the same indentation depth of 4.0 nm. Figures 4(a)–4(c), respectively, show the shear strain of two layers of atomic bonds at the intermediate interface perpendicular to the x -axis with indentation planes (001), (110), and (111), and (d)–(f), respectively, show the shear strain of two layers of atomic bonds at the intermediate interface perpendicular to the y -axis with indentation planes (001), (110), and (111). Figures 4(g)–4(i) show the overall dislocation bond shear strain diagrams with indentation planes of (001), (110), and (111), respectively. In Figures 4(a) and 4(d), there is no weak strain region in the center of the indentation defect due to the increase of shear strain, and the newly generated shear strain near the indentation defect forms multiple closed-loop loops. With the increase of indentation depth, a large number of cross dislocation rings are generated on the outer wall of indentation defects (as shown in Figure 4(g)). When the indentation depth is 4 nm, the two shear strain chains in Figures 4(b) and 4(e) are increased compared with that when the indentation depth is 2 nm, and a large number of horizontal dislocation rings are generated outside the indentation defects (as shown in Figure 4(h)). In Figure 4(c), the strong shear strain region on the left expands more than when the indentation depth is 2 nm, and a strong strain chain is generated along the oblique structure. In Figure 3(f), there is a strain closed loop on both sides of the indentation defect. With the increase of the indentation depth, a new strain closed loop is added above it (as shown in Figure 4(f)). Finally, the previously formed dislocation ring slides below to form a horizontal dislocation, while the newly formed dislocation is a vertical dislocation (as shown in Figure 4(i)).

3.3. Effect of Different Crystal Planes on Dislocations.

Figure 5 shows the atomic deformation process of 3C-SiC (001) crystal surface during nanoindentation of cube indenter. In order to visually show the deformation process

of atoms, 3C-SiC specimens with a height from 85 Å to 150 Å are colored and distinguished according to the height. When the indentation depth is 1.4 nm, as shown in Figure 5(a), the first vertical dislocation ring is generated at a right angle of the square indentation defect. The deformation of silicon carbide changes from elastic deformation to irreversible plastic deformation. The Berger vector of the dislocation ring is $b = 1/2[1\bar{1}0]$. When the indentation depth is 1.6 nm, as shown in Figure 5(b), the atoms under the indentation defect slip and produce a new dislocation ring sliding along the $[10\bar{1}]$ crystal direction. With the increase of indentation depth, the range of atomic slip becomes larger and larger, and the dislocation ring expands outward (as shown in Figure 5(c)). When the indentation depth is 2.0 nm, as shown in Figure 5(d), the dislocation ring continues to expand, and both ends of the dislocation ring extend below both ends of the square indentation defect. When the indentation depth is 2.2 nm, as shown in Figure 5(e), a large number of atoms slip, $b = 1/2[1\bar{1}0]$ and $b = 1/2[10\bar{1}]$ the two dislocation rings with Berger vector sum continue to expand, cross and collide, and finally, connect together. This is because with the atomic slip, the shear strain concentrates and gradually increases, the bond angle between the atoms of the dislocation ring formed under the indenter breaks, and the adjacent atoms recombine to form a new chemical bond, so that the two dislocation rings are finally combined together. A new dislocation ring is also generated below the boundary of the square indentation defect, and its Berger vector is $b = 1/2[0\bar{1}1]$. When the indentation depth is 2.4 nm, as shown in Figure 5(f), the atoms are subjected to excessive stress, which will lead to the fracture of atomic bonds and reorganization to form dislocation rings. The three dislocation rings connected together fuse into a large dislocation ring with a Berger vector of $b = 1/2[1\bar{1}0]$, and a new small dislocation ring is generated, sliding along the $[\bar{1}01]$ crystal direction. In the whole indentation process, the direction of dislocation propagation is $\langle 110 \rangle$ crystal direction group, and atoms are easy to slip to $\langle 110 \rangle$ crystal direction group.

Figure 6 shows the atomic deformation process of 3C-SiC (110) crystal surface during nanoindentation of cube indenter. When the indentation surface is (110) crystal surface, the x -axis direction is $[001]$ crystal direction, the y -axis direction is $[1\bar{1}0]$ crystal direction, and the z -axis direction is $[110]$ crystal direction. When the indentation depth is 0.9 nm, as shown in Figure 6(a), the 3C-SiC specimen is elastically deformed without dislocation ring. A small number of atoms under the two opposite sides of the square indentation defect slide along the negative direction of the z -axis, which is far from the deformation in the middle region. When the indentation depth is 1.2 nm, as shown in Figure 6(b), a large number of atoms under the right boundary of the indentation defect slip to produce the first dislocation nucleation, and its Berger vector is $b = 1/2[112]$. This is the initial stage of dislocation nucleation. When the indentation depth is 1.5 nm, as shown in Figure 6(c), the first dislocation ring expands continuously, and a new dislocation ring is generated below the left boundary of the indentation defect. Its sliding direction is opposite to that of the first

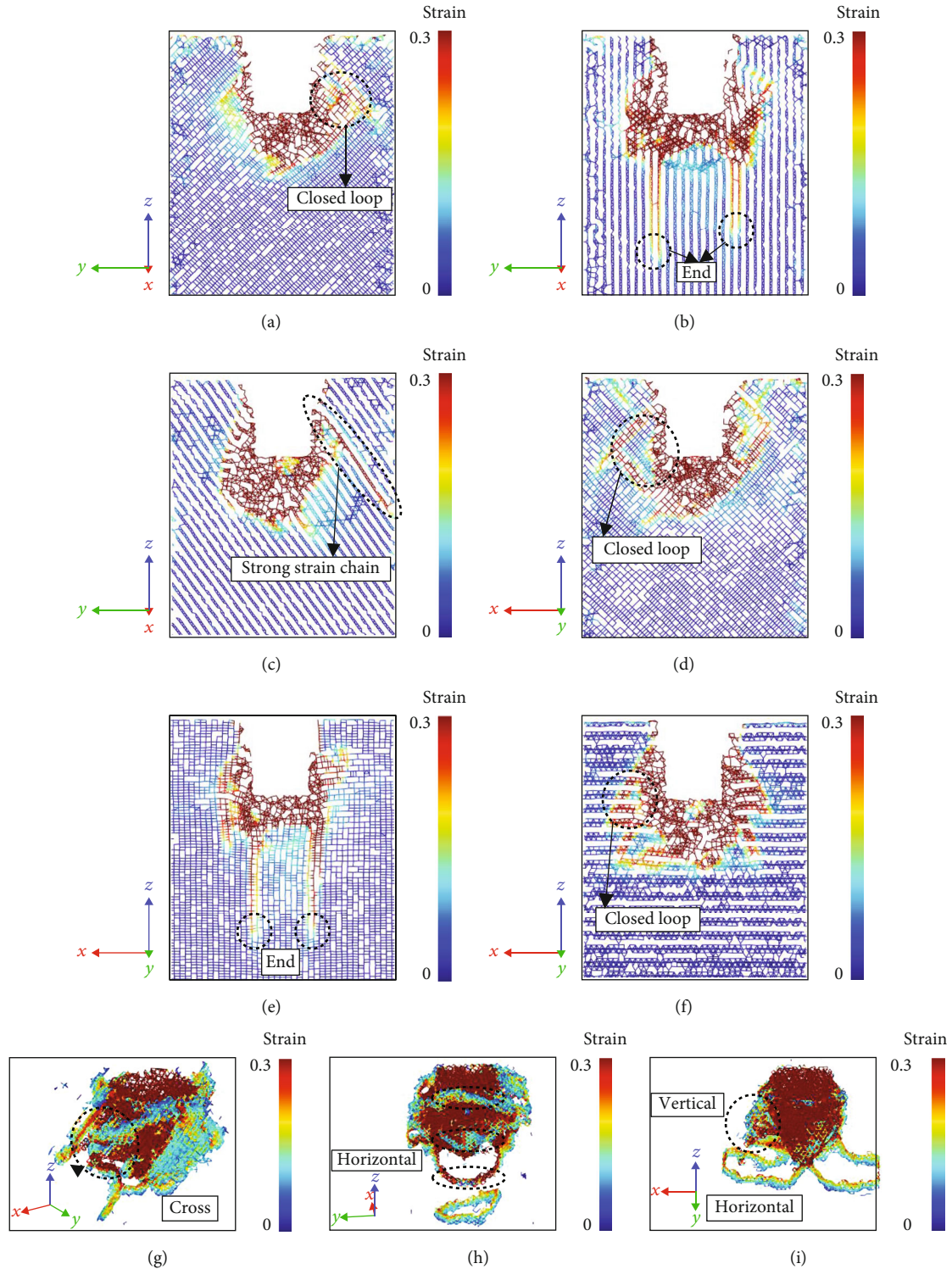


FIGURE 4: Shear strain nephogram at indentation depth of 4.0 nm.

dislocation ring, and its Berger vector is $b = 1/2[\bar{1}\bar{1}\bar{2}]$. When the indentation depth is 1.8 nm, as shown in Figure 6(d), the dislocation rings on both sides of the indentation defect expand outward to form two horizontal dislocations. Both ends of each dislocation ring slip to the middle, and finally, cross together to form two intersections. When the indenta-

tion depth is 2.1 nm, as shown in Figure 6(e), the two ends of the two dislocation rings are connected together at the intersection and disconnected from the main body, resulting in dislocation cutting. A single and complete rectangular dislocation ring is formed, and its Berger vector is $b = 1/2[112]$. With the continuous increase of indentation depth, the

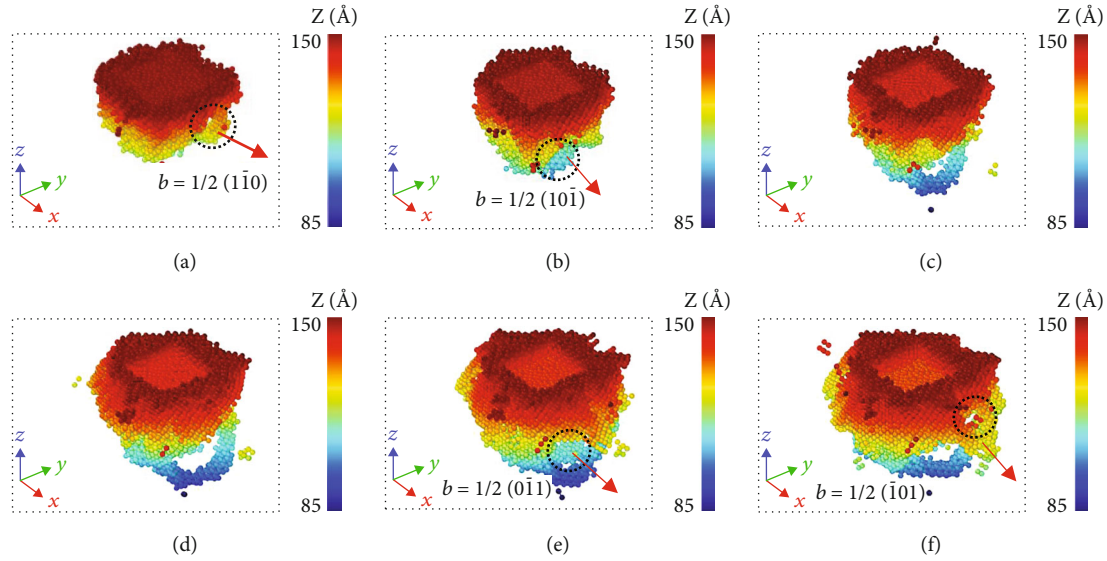


FIGURE 5: Deformation process of 3C-SiC (001) crystal surface with different indentation depths. (a) 1.4 nm, (b) 1.6 nm, (c) 1.8 nm, (d) 2.0 nm, (e) 2.2 nm, and (f) 2.4 nm.

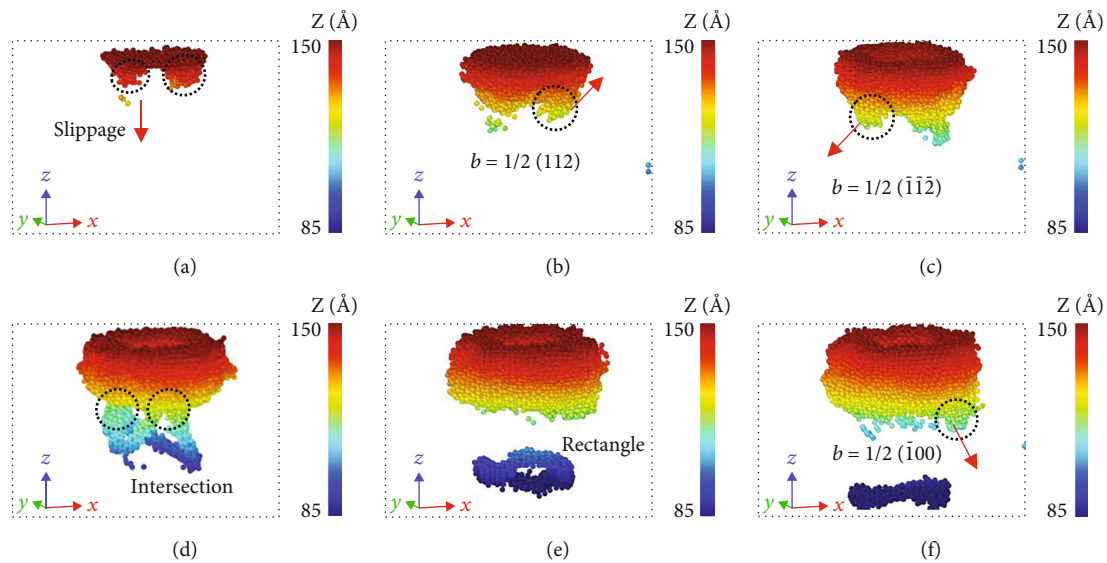


FIGURE 6: Deformation process of 3C-SiC (110) crystal surface with different indentation depths. (a) 0.9 nm, (b) 1.2 nm, (c) 1.5 nm, (d) 1.8 nm, (e) 2.1 nm, and (f) 2.4 nm.

rectangular dislocation ring continues to move in the negative direction of z -axis, and a new dislocation ring is generated in the main part, with its Berger vector $b = 1/2[100]$ as shown in Figure 6(f). When the indentation surface is (110) crystal surface, the shape of the contact between the indenter and the crystal surface can affect the shape of the downward moving dislocation ring.

Figure 7 shows the atomic deformation process of 3C-SiC (111) crystal surface during nanoindentation of cube indenter. When the indentation surface is (111) crystal surface, its x -axis direction is $[11\bar{2}]$ crystal direction, y -axis direction is $[\bar{1}2\bar{1}]$ crystal direction, and z -axis direction is $[111]$ crystal direction. When the indentation depth is 0.8 nm, as shown in Figure 7(a), the first dislocation ring is generated. Both ends of the dislocation ring are, respectively,

below a pair of right angles of the square indentation defect, and its Berger vector is $b = 1/2[\bar{1}2\bar{1}]$, sliding along the positive direction of the y -axis. When the indentation depth is 1.2 nm, as shown in Figure 7(b), one end of the first dislocation ring slides to the left while expanding, and the second dislocation ring is generated at another pair of right angles of the square indentation defect, and its Berger vector is $b = 1/2[152]$. When the indentation depth is 1.6 nm, as shown in Figure 7(c), a large number of atoms under the defect slip, which produces large shear strain on the surrounding atoms and makes the dislocation expand outward. One end of the first dislocation continues to slide to the left, and one end of the second dislocation slides to the right. A third dislocation ring is generated under one edge of the square indentation defect, and its Berger vector is $b = 1/2[\bar{1}10]$. When the

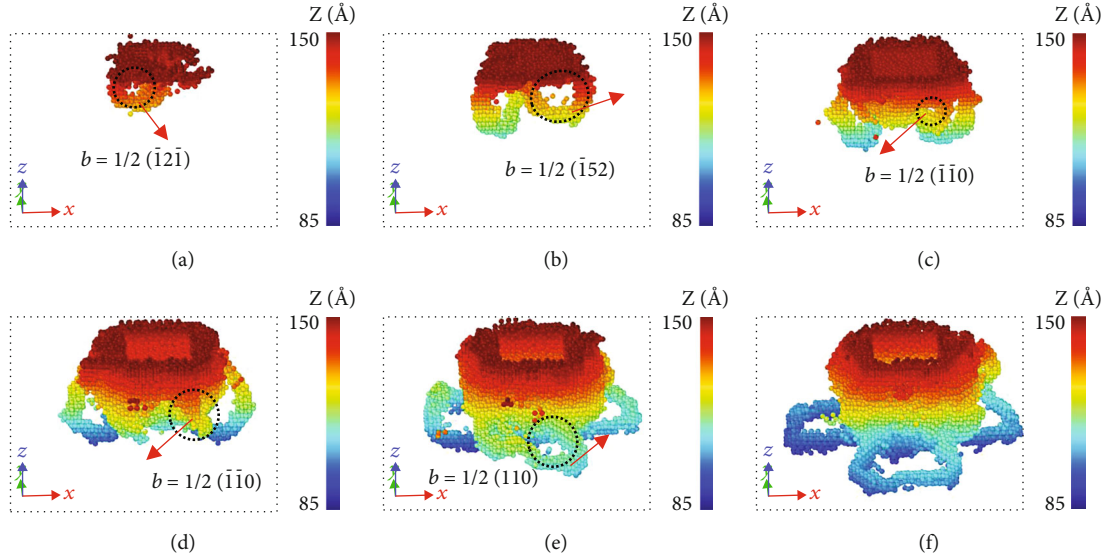


FIGURE 7: Deformation process of 3C-SiC (111) crystal surface with different indentation depths. (a) 0.8 nm, (b) 1.2 nm, (c) 1.6 nm, (d) 2.0 nm, (e) 2.4 nm, and (f) 2.8 nm.

indentation depth is 2.0 nm, as shown in Figure 7(d), with the increase of indentation depth, the three dislocation rings continue to expand in three different directions. The two ends of the first and second dislocation rings are close to each other at the same time, and the third dislocation ring slides to the middle. When the indentation depth is 2.4 nm, as shown in Figure 7(e), the two ends of the first and second dislocation rings intersect and converge under two right angles, respectively, one end of the third dislocation ring diffuses to the left to the other right angle, and the distance between its two ends is the side length of the square indentation defect. In the process of diffusion, its Berger vector changes, which is $b = 1/2[110]$. When the indentation depth is 2.8 nm, as shown in Figure 7(f), the dislocation loop expands and decreases, and finally, three square like closed loops are formed.

4. Conclusion

(1) Through the molecular dynamics simulation of nanoindentation, the effects of indentation depth on atomic spacing and staggered deformation at high temperature are explored. In the process of indentation, the atomic spacing in the crystal decreases continuously. At the initial stage of indentation, the SiC specimen is elastically deformed and the atomic spacing changes rapidly. With the increase of indentation depth, dislocations occur in the specimen, and the change rate of atomic spacing slows down, and finally, remains stable. When the first dislocation ring is generated, the SiC specimen changes from elastic deformation to plastic deformation. Due to the small indentation depth, there is no brittle deformation. The atoms of dislocations continue to slide around, and the dislocations cross and fuse with each other to form new dislocations

(2) In the process of nanoindentation, the shear strain and dislocation in the crystal are different due to different crystal planes. When the indentation surface is the (001) crystal surface, there is a weak strain region below the center of the square indentation defect, and the strong strain region is below the boundary, so that the four right angles of the indentation defect are easy to produce dislocation rings, forming a variety of dislocation rings surrounding the defect with the lower right angle as the endpoint. When the indentation plane is (110) crystal plane, the shear strain increases along the $[\bar{1}\bar{1}0]$ crystal direction at both ends of the indentation defect, resulting in the formation of a closed rectangular dislocation ring directly below the indentation defect. When the indentation surface is (111) crystal surface, there is a weak strain region below the center of the indentation defect, and the shear stress is released to the periphery along the atomic bond structure. Under the action of stress and strain, three square-like closed loops are formed under three edges of the square indentation defect

(3) Nanoindentation is of great significance in precision machining. When the indentation plane is (001) crystal plane, there is no separated dislocation ring due to the influence of internal structure. Atomic slip and dislocation are confined around the indentation, so that the shear strain is concentrated around the indentation, and the shear strain is large. In the actual indentation process, it is difficult to process, but the internal atomic arrangement is least affected by indentation. When the indentation surface is (110) crystal surface, two downward extending shear strains will be generated to effectively release the shear stress. It is easier to process than when the indentation surface is (001) crystal surface. The

arrangement of atoms in the vertical direction of the indentation position is affected by the indentation process. When the indentation plane is (111) crystal plane, the outward shear strain also occurs, and the dislocation occurs the earliest. Dislocation loops have been generated when the indentation depth is 0.8 nm. Among the three different crystal planes, the silicon carbide with the indentation surface of (111) crystal plane is the easiest to process, and the silicon carbide with the indentation surface of (110) crystal plane has better penetration due to the vertical downward sliding of atoms, and the silicon carbide with the indentation surface of (001) crystal plane is the most difficult to process

Data Availability

No data were used to support this study.

Conflicts of Interest

The authors declare that they have no conflicts of interest.

Acknowledgments

This work is supported by the National Natural Science Foundation of China (grant no. 51964022), the Natural Science Youth Fund of Jiangxi Province (grant no. 20212BAB214033), and the Jiangxi Provincial Natural Science Key Fund (grant no. 20212ACB204012).

References

- [1] M. Striegler, B. Matthey, U. Mühle, A. Michaelis, and M. Herrmann, "Corrosion resistance of silicon-infiltrated silicon carbide (SiSiC)," *Ceramics International*, vol. 44, no. 9, pp. 10111–10118, 2018.
- [2] Y. Yao, X. Zeng, G. Pan et al., "Interfacial engineering of silicon carbide nanowire/cellulose microcrystal paper toward high thermal conductivity," *ACS Applied Materials & Interfaces*, vol. 8, no. 45, pp. 31248–31255, 2016.
- [3] A. S. Rashid, M. S. Islam, N. Ferdous, K. N. Anindya, J. Park, and A. Hashimoto, "Widely tunable electronic properties in graphene/two-dimensional silicon carbide van der Waals heterostructures," *Journal of Computational Electronics*, vol. 18, no. 3, pp. 836–845, 2019.
- [4] X. She, A. Q. Huang, O. Lucia, and B. Ozpineci, "Review of silicon carbide power devices and their Applications," *IEEE Transactions on Industrial Electronics*, vol. 64, no. 10, pp. 8193–8205, 2017.
- [5] A. Akturk, J. M. McGarrity, N. Goldsman et al., "Predicting cosmic ray-induced failures in silicon carbide power Devices," *IEEE Transactions on Nuclear Science*, vol. 66, no. 7, pp. 1828–1832, 2019.
- [6] W. W. Xu, F. Xia, L. Chen, M. Wu, T. Gang, and Y. Huang, "High-temperature mechanical and thermodynamic properties of silicon carbide polytypes," *Journal of Alloys and Compounds*, vol. 768, pp. 722–732, 2018.
- [7] S. Singh, K. Rathi, and K. Pal, "Synthesis, characterization of graphene oxide wrapped silicon carbide for excellent mechanical and damping performance for aerospace application," *Journal of Alloys and Compounds*, vol. 740, pp. 436–445, 2018.
- [8] A. V. Kostanovskiy, M. G. Zeodinov, M. E. Kostanovskaya, and A. A. Pronkin, "Emittance properties of siliconized silicon carbide in the temperature range of 1400–2200 K," *High Temperature*, vol. 57, no. 2, pp. 272–274, 2019.
- [9] J. Chen, J. Shi, M. Zhang et al., "Effect of indentation speed on deformation behaviors of surface modified silicon: A molecular dynamics study," *Computational Materials Science*, vol. 155, pp. 1–10, 2018.
- [10] Q. Sun, M. Yang, J. Li et al., "Heteroepitaxial growth of thick 3C-SiC (110) films by LaserCVD," *Journal of the American Ceramic Society*, vol. 102, no. 8, pp. 4480–4491, 2019.
- [11] L. L. Snead, Y. Katoh, T. Koyanagi, K. Terrani, and E. D. Specht, "Dimensional isotropy of 6H and 3C SiC under neutron irradiation," *Journal of Nuclear Materials*, vol. 471, pp. 92–96, 2016.
- [12] I. S. Aisyah, M. Wyszomirska, A. Calka, and D. Wexler, "Rapid transformation of hexagonal to cubic silicon carbide (SiC) by electric discharge assisted mechanical Milling," *Plasma Chemistry and Plasma Processing*, vol. 36, no. 4, pp. 1177–1186, 2016.
- [13] P. Zhou, X. Shi, J. Li et al., "Molecular dynamics simulation of SiC removal mechanism in a fixed abrasive polishing process," *Ceramics International*, vol. 45, no. 12, pp. 14614–14624, 2019.
- [14] A. V. Redkov, A. V. Osipov, and S. A. Kukushkin, "Molecular dynamics simulation of the indentation of nanoscale films on a substrate," *Technical Physics Letters*, vol. 42, no. 6, pp. 639–643, 2016.
- [15] B. Zhu, D. Zhao, and H. Zhao, "A study of deformation behavior and phase transformation in 4H-SiC during nanoindentation process via molecular dynamics simulation," *Ceramics International*, vol. 45, no. 4, pp. 5150–5157, 2019.
- [16] L. Zhao, M. Alam, J. Zhang, R. Janisch, and A. Hartmaier, "Amorphization-governed elasto-plastic deformation under nanoindentation in cubic (3C) silicon carbide," *Ceramics International*, vol. 46, no. 8, pp. 12470–12479, 2020.
- [17] L. Zhao, J. Zhang, J. Zhang, and A. Hartmaier, "Atomistic investigation of machinability of monocrystalline 3C-SiC in elliptical vibration-assisted diamond cutting," *Ceramics International*, vol. 47, no. 2, pp. 2358–2366, 2021.
- [18] Z. Wu and L. Zhang, "Mechanical properties and deformation mechanisms of surface-modified 6H-silicon carbide," *Journal of Materials Science and Technology*, vol. 90, pp. 58–65, 2021.
- [19] K. H. Pang, R. Zhou, and A. Roy, "Deformation characteristics in micromachining of single crystal 6H-SiC: insight into slip systems Activation," *Journal of Mechanics*, vol. 36, no. 2, pp. 245–253, 2020.
- [20] A. J. Leide, R. I. Todd, and D. E. J. Armstrong, "Effect of ion irradiation on nanoindentation fracture and deformation in silicon Carbide," *JOM: the journal of the Minerals, Metals & Materials Society*, vol. 73, no. 6, pp. 1617–1628, 2021.
- [21] P. Erhart and K. Albe, "Analytical potential for atomistic simulations of silicon, carbon, and silicon carbide," *Physical Review B*, vol. 71, no. 3, pp. 1–14, 2005.
- [22] P. Vashishta, R. K. Kalia, A. Nakano, and J. P. Rino, "Interaction potential for silicon carbide: a molecular dynamics study of elastic constants and vibrational density of states for crystalline and amorphous silicon carbide," *Journal of Applied Physics*, vol. 101, no. 10, p. 103515, 2007.